Finite element-based optimisation of an elastomeric honeycomb for impact mitigation in helmet liners

Rhosslyn Adams[1], *Scott Townsend*[1], *Shwe Soe*[2], *Peter Theobald*[1*]

[1] School of Engineering, Cardiff University, UK

[2] Department of Engineering, Design and Mathematics, University of the West of England, UK

* Corresponding author. E-mail: TheobaldPS@Cardiff.ac.uk

Keywords

Honeycomb; optimisation; finite element analysis; impact; helmet; additive manufacturing

Abstract

Finite element simulation was used to analyse the response of an elastomeric pre-buckled honeycomb structure under impact loading, to establish its suitability for use in helmet liners. A finite element-based optimisation was performed using a search algorithm based on a radial basis function. This approach identified optimisation configurations of a pre-buckled honeycomb structure, based on structural bounds subject to impact loading conditions. Furthermore, the influence of objective function, peak acceleration and head injury criterion was analysed with respect to the resultant mechanical behaviour of the structure. Numerical results demonstrate that this class of structure can exceed the performance threshold of a common helmet design standard and minimise the resultant injury index. Experimental testing, facilitated through laser sintering of thermoplastic polyurethane powder, validated the output of the numerical optimisation. When subject to initial impact loading, the fabricated samples satisfied their objective functions. Successive impact loading was performed to assess the performance and degradation. Samples optimised for peak acceleration demonstrated superior performance after stabilisation, relative to their initial response. The culmination of this study establishes a numerical design pathway for future optimisation of candidate structures for head impact protection. Furthermore, the optimised pre-buckled honeycomb structure represents a new class of energy absorbing structure, which can exceed the thresholds prescribed by the design standard.

1. Introduction

Physical activity that includes elevation or speed carries the risk of head injury. Injury risk is mitigated by wearing safety helmets [1], [2], [3]. Whilst cycling is adopted as an exemplar when evaluating new helmets [4], [5] and their use being advocated by the World Health Organisation [6], head injury remains a notable cause of mortality and morbidity in cycling accidents [7], [8]. Indeed, head injury still causes 69-93% of fatal bicycle accidents [9]; hence, new helmet technologies remain of significant social importance.

Advances in computational modelling and additive manufacturing (AM) have enabled investigation of novel alternative helmet liners that can exceed contemporary materials performance (e.g., Polymeric Foam). *Soe et. al* numerically explored the use of an ordered lattice structure for impact mitigation [10], demonstrating that tailorable energy absorption and thus impact mitigation can be achieved through structural changes. This concept has since been expanded by *Khosroshahi et. al,* who investigated lattice grading schemes and relative density on head injury severity [11], [12]. *Clough et. al* fabricated micro lattice impact attenuators, which afforded greater specific stiffness and densification strain, resulting in a reduction in peak linear acceleration under impact versus stochastically architecture foams [13]. The greater geometric freedom means architectured cellular structures hold a notable advantage over stochastic cellular structures. Architectured cellular structures with tailorable mechanical properties, therefore, represent a viable route to improving helmet liner performance and ultimately head protection.

The honeycomb is another example of an architecture cellular structure [14]. Combing properties such as high specific strength and stiffness [15], and excellent impact mitigating properties [16], the honeycomb has become a common design route to achieve lightweight structures with high energy absorption [17], [18]. The adoption of honeycomb structures within helmet design can improve user safety [19], [20]. Localised reinforcement [21], [22], exclusive use [23], or a hybrid combination of foam and honeycombs [24] provide superior performance relative to a monolithic equivalent. In all cases, the principal mechanisms leveraged to mitigate the impact energy are plastic deformation and material fracture. These solutions are unsuitable for applications with potential for multiple (or consecutive) impacts however, as the onset of permanent deformation will diminish helmet performance [25]. Indeed, it is common for consumers to wear a previously damaged helmet despite contrary advice [26]; hence, there is growing motivation in identifying a multi-impact solution [27].

In recent years, elastically recoverable honeycomb structures have been investigated due to the potential of repeatable and high specific energy absorption. Furthermore, elastomers can now be additively manufactured, facilitating rapid design exploration of novel structures that are infeasible using traditional methods such as injection moulding [28]. *Bates et. al*, for example, reported that hexagonal honeycombs additively manufactured from thermoplastic polyurethane achieved recoverable behaviour under cyclic compression, whereby the behaviour of these structures could be tailored by changing the unit cell structure [29], [30]. *Adams et. al* investigated the dynamic response of elastomeric pre-buckled honeycombs, reporting a stabilised yield stress and energy absorption following repeat impact loading [31]. *Townsend et. al* investigated the tailorable energy absorption of elastomeric origami-inspired honeycombs, reporting the potential application for helmet liners [32]. *Caccese et. al* is one of few studies describing design optimisation using intelligent search algorithms of elastomeric honeycombs, presenting optimal elastomeric honeycomb structures for head impact mitigation [33]. Adopting a simplified genetic search algorithm, minimum unit cell depth could be identified to achieve a reduced peak acceleration. Loading conditions equivalent to the design certification standards for head protection were not adopted however [34], meaning further investigation is required under these conditions to establish whether this class of structure can satisfy the performance requirement.

A novel additively manufactured elastomeric pre-buckled honeycomb structure has demonstrated excellent energy absorption capability during quasi-static and dynamic testing over successive loading cycles [31]. This study aims to optimise the honeycomb structure subject to the loading conditions and performance threshold of the design standard for cycling helmets. A numerical approach is outlined that utilises a finite element-based optimisation to identify the optimal honeycomb configuration. Moreover, the influence of varying objective function is also evaluated. Laser sintering of a thermoplastic polyurethane powder is adopted to fabricate the optimal structures, which were experimentally tested under equivalent conditions to enable validation of the numerical approach. Lastly, successive impact testing is carried out to establish the performance degradation over multiple impacts. The outcome of this study is a numerical design pathway for optimisation of candidate structures for impact mitigation.

2. Materials & Methods

The design of the proposed pre-buckled honeycomb is presented with respect to its structural parameters. The finite element model used to simulate impact loading is then discussed providing the basis for optimisation. The sequential steps of the search algorithm are then described, followed by an overview of the computational sequence. Lastly, the fabrication and testing of optimal honeycombs is detailed.

2.1 Honeycomb structure

A circular pre-buckled honeycomb structure (figure 1) was defined by structural parameters: cell size (w), wall thickness (t), depth (d), circular minor radius (r_1), circular major radius (r_2), and number of folds (f). The aspect ratio (e), hereafter used to describe the eccentricity of the circular cross section of the unit cell, is defined as the ratio of r_1 and r_2. The fold is based on a cosine function. Computer aided design files for fabrication and simulation were generated using an in-house code written in Python [31].

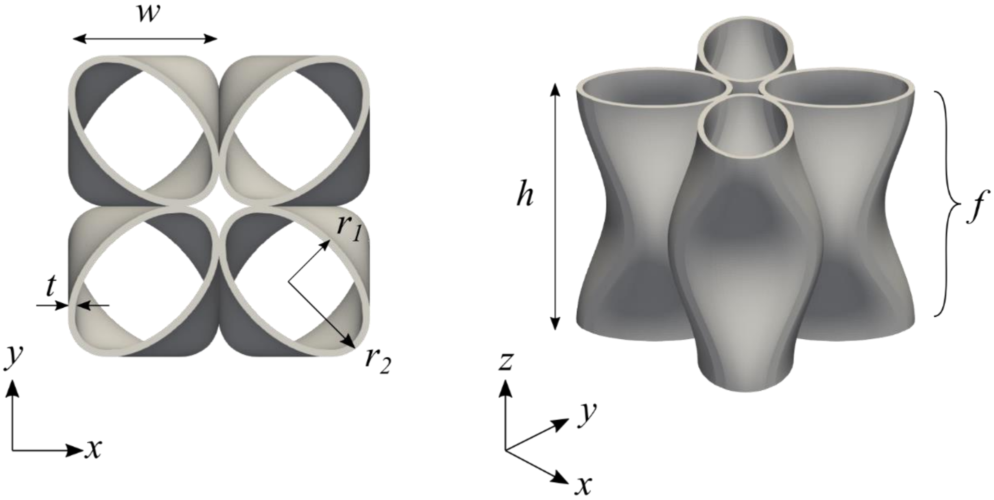

Figure 1: The structural model of the pre-buckled honeycomb unit cell including parameters cell size (w), wall thickness (t), depth (d), circular minor radius (r_1), circular major radius (r_2) and number of folds (f).

2.2 Finite element model

Finite element analysis (Abaqus Explicit 2019; Dassault Systems, France) was performed to replicate the shock absorption test from the cycling helmet design standard EN1078 [35]. The model comprised a deformable honeycomb comprising of two unit cells positioned between two analytically rigid plates as illustrated by figure 2.

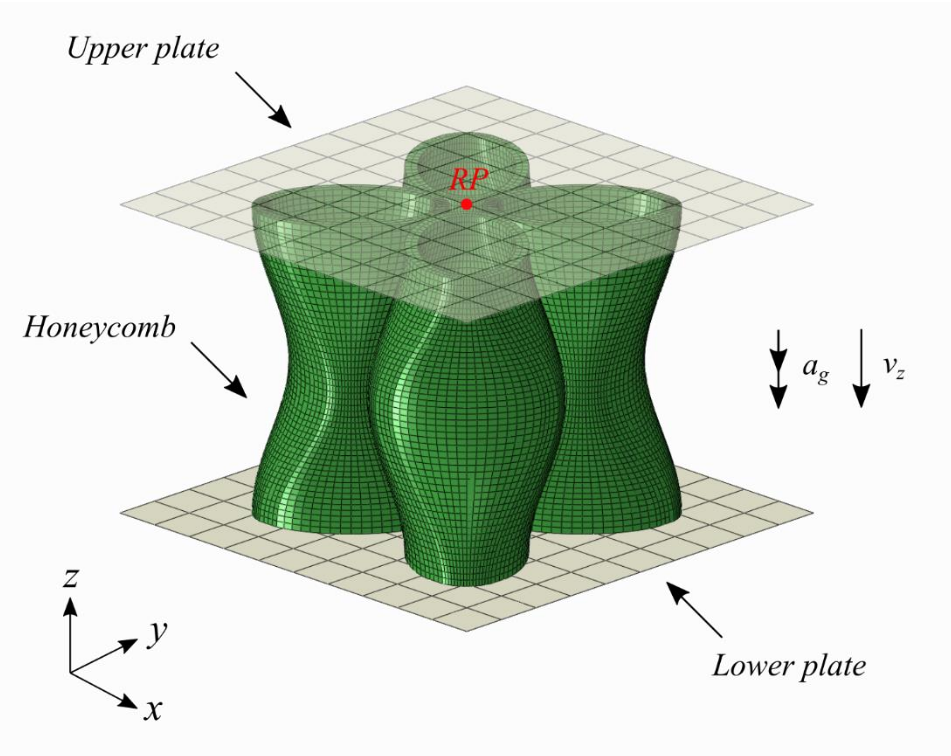

Figure 2: The finite element model of the pre-buckled honeycomb comprising of two unit cells positioned between an upper and lower rigid plate. The upper plate is assigned a pre-impact velocity and point mass, whilst the lower is fixed.

The lower plate was assigned an encastre boundary condition and the upper plate a point mass of 4.7kg, equivalent to a size J headform [36]. Pre-impact velocity of $v_z = 5.42ms^{-1}$ was adopted from the design standard, whilst global acceleration due to gravity, $a_g = 9.81ms^{-2}$ was assigned to the entire model. This represents the experimental setup (section 2.5) enabling validation of the numerical outcome, whilst simplifying the anticipated crushing between the head and the liner under impact.

An efficient periodic boundary condition model alleviated the computational cost of multiple full-scale simulation. In the model, the 2 x 2 honeycomb configuration has zero displacement in the X and Y axes along the perimeter nodes. The lower plate boundary conditions remained the same, whilst the upper plate point mass was scaled by 0.25, proportional to the kinetic energy, to account for load distribution over a quarter of the projected area. Previous work validated this approach, reporting it as comparable to 4 x 4 honeycomb array under impact loading [31].

An eight-node brick element with hexahedron shape type, reduced integration and hourglass controlled was utilised (C3D8R). The mesh density was selected so that there were two elements across the wall thickness to mitigate against shear locking; mesh independence studies identified diminishing gains using greater than two elements. A global friction value of 1.0 was used to emulate the anticipated friction that arises from self-contact of the elastomeric material, in accordance with similar studies [31], [32]. Although this global friction is not likely to represent the surface contact between the plates and honeycomb, it is considered an acceptable simplification due to the relatively small contact area. Luvosint was adopted as the base material, a thermoplastic polyurethane utilised in additive manufacturing (e.g., laser sintering), with a density of 1200kg/m^3. Material behaviour was characterised under uniaxial, planar and equiaxial tension, as well as single step stress relaxation and is described in figure 3. The numerical material model was validated under quasi-static and dynamic, isolated and mixed deformation testing [37], [38]. An isotropic Ogden N5 material model was used to represent the non-linear hyperelastic behaviour, which was then augmented with a linear viscoelastic material model, Prony series, to represent the rate dependant behaviour (material model coefficients are reported in the appendix, table A1 and A2 respectively). Initial honeycomb impact tests indicated no obvious structural fracture nor material plasticity; therefore, fracture and damage was not considered in the numerical simulations. Furthermore, whilst it is well known that additive manufacturing's layer by layer process yields a degree of local anisotropy with respect to the build direction, this was not considered in the numerical analysis as the mechanical behaviour is recognised to be less sensitive when exposed to compressive loads in line with the build axis [39].

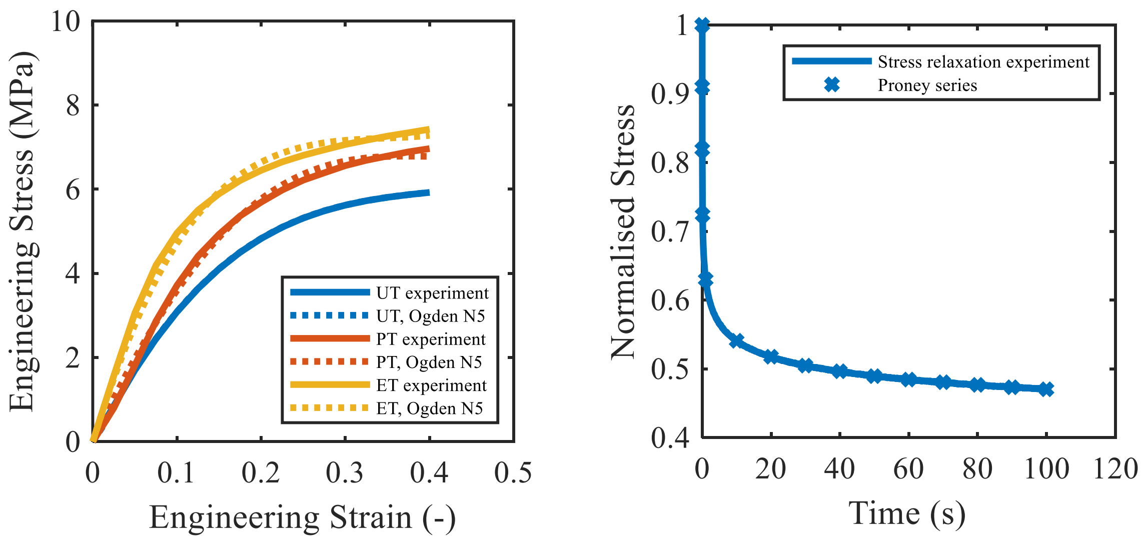

(a) Uniaxial (UT), planar (PT) and equibiaxial tension (ET) experiment compared to material model

(b) Stress-relaxation experiment compared to material model

Figure 3: Mechanical behaviour of the sintered Luvosint under three modes of deformation and stress relaxation used in the calibration of the hyperelastic and linear viscoelastic model respectively. Adopted from [37].

A 15ms simulation time was used to sufficiently capture the entirety of the impact event. Reaction force, linear acceleration, and velocity, as well as displacement in the Z-axis was recorded with respect to time and extracted from the reference point located on the upper surface. This was then used to calculate the dynamic stress and strain at the reference point. Stress was calculated by dividing the reaction force by the projected cross-sectional area and strain by normalising the plate displacement by the honeycomb height. The recorded data was further treated with a low pass Butterworth filter that had a 1000Hz cut-off frequency. Head injury criterion (HIC) was also calculated, using equation (1), to establish the relative severity of the resultant acceleration [40]. Since there was no rotational kinematics induced during the impact, rotational severity indexes were not considered.

$$HIC = max\left[\frac{1}{t_2 - t_2}\int_{t_1}^{t_2} a(t)\,dt\right]^{2.5}(t_2 - t_1) \qquad (1)$$

2.3 Optimisation

To identify the ideal honeycomb parameters for impact mitigation, numerical optimisation was performed based on a finite number of simulations using the surrogate optimisation algorithm available in MATLAB's Optimisation Toolbox (MathWorks, United States). The surrogate optimisation algorithm, which is based on a radial basis function [41], was adopted over other search algorithms available in MATLAB, such as genetic, particle swarm or simulated annealing due to its capability of accurately modelling arbitrary functions, handling scattered training points in multiple dimensions and requiring fewer iterations [42]. Moreover, since it is a non-gradient based solver, it is more appropriate for problems that include discontinuities due to self-contact. Lastly, it is more suited to time-consuming objective functions, such as finite element problems, as it is proven to converge to a global optimum for bounded problems.

The surrogate optimisation algorithm occurs over multiple steps, as illustrated by figure 4. Initially, quasi-random points are sampled throughout the design space, with the objective function evaluated following each successful design point simulation. The surrogate, which approximates the relationship between each design point and the objective function, is then constructed by interpolating a cubic spline with a linear tail through the sampled points. Next, the algorithm searches for the minimum. New values are sampled within the design space around the incumbent value. A merit function is evaluated subject to the surrogate model values at these points, as well as the distance between them and the points where the objective function has already been evaluated. The best point, based on its merit function, is simulated and the objective function evaluated. The surrogate model is then updated to reflect the new information. This cycle repeats for a finite number of iterations where the fidelity of the surrogate model improves. Upon convergence, the surrogate model is reset, and new random samples selected to ensure the design space is fully explored. Once the maximum number of iterations is reached, the minimum point can be identified.

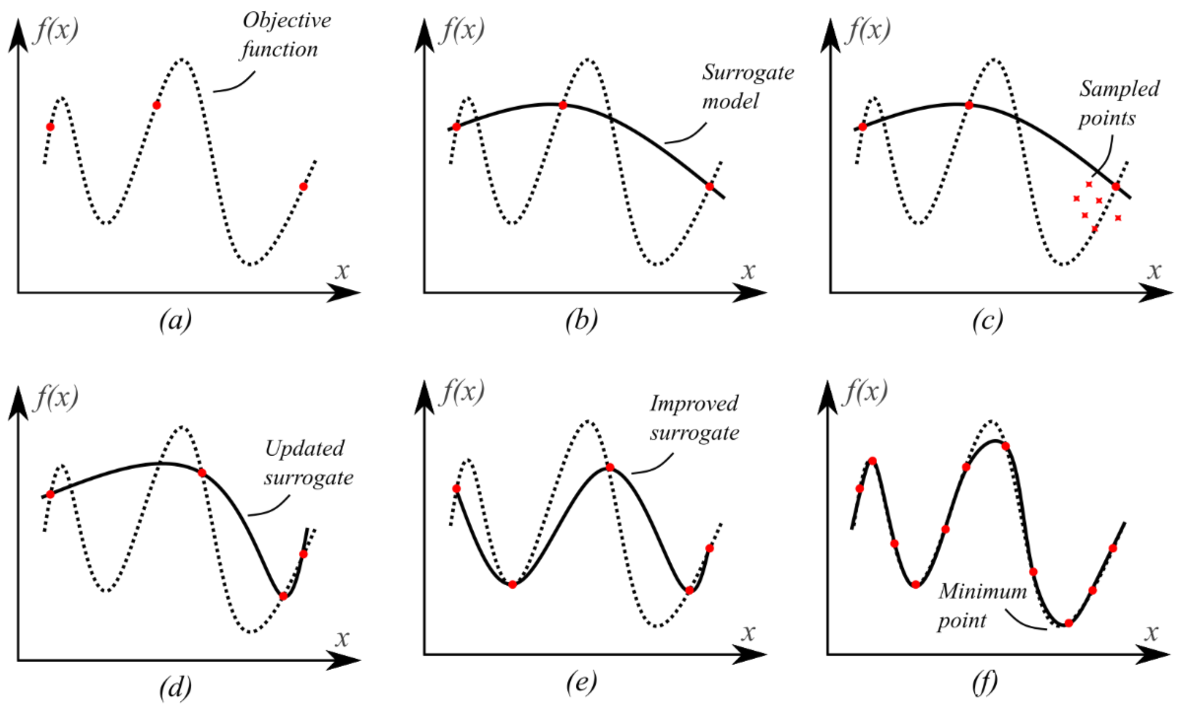

Figure 4: The optimisation steps for construction of the surrogate response used by the search algorithm for an increasing number of sampled finite element simulations including, (a) random sampling, (b) surrogate construction, (c) merit function analysis, (d) best point simulated, (e) surrogate model updated and (f) final surrogate model approximation.

The objective function used in this optimisation was adopted from the cycle helmet design standard (EN1078), which defines an acceptable shock absorption threshold. The standard mandates that, for a singular impact, the resultant acceleration shall not exceed 250g [35]. Consequently, the objective function was defined by equation (2).

$$f(x_d) = \frac{J_{calc}}{J_{crit}} \qquad (2)$$

Where f(x) is the objective function, x is the structural parameter vector, J_{calc}, is the calculated objective function recorded during the simulation, normalised by J_{crit} a critical threshold value. The optimisation problem is therefore defined by the number of structural parameters, x, the constructed surrogate model, and subject to structural parameter limits described as follows:

$Find: t, e$

$Minimise: f(x)$

$Subject\ to: w = 12.5mm, d = 25.0mm,\ 0.8mm \leq t \leq 1.4mm,\ 0.6 < e < 0.8,\ f = 1.0$

To utilise the optimisation approach, a computational procedure was developed. As illustrated by figure 5, Matlab, Python and Abaqus, were utilised to execute the structural optimisation. Initially, user-specified inputs such as maximum number of iterations, loading conditions (mass and velocity) and structural parameter limits were set. The optimisation search algorithm was then initiated using Matlab. The structural parameter vector was parsed, and a Python script was called that meshed the structure. A secondary script consisting of indigenous Abaqus macros imported the newly meshed configuration, applied boundary conditions and wrote the simulation job file. Once the new job file was written, Matlab executed the job. Upon completion of the simulation, the result file was automatically analysed and filtered using another Python script, before being imported into Matlab which calculated the objective function. This procedure was then repeated where the structural parameter vector changes with respect to the calculated objective function. Once the user prescribed iteration limit was reached, the procedure ends.

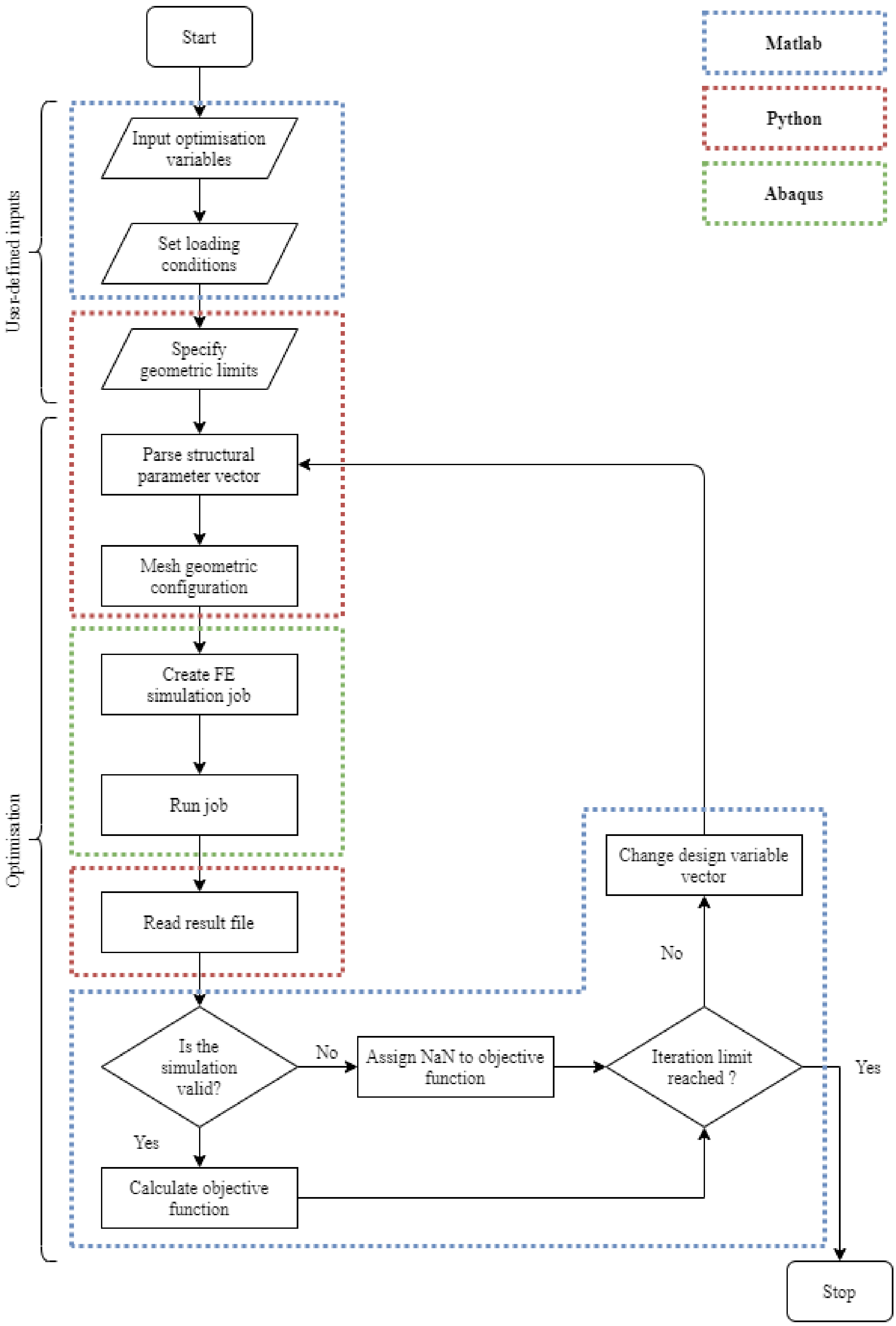

Figure 5: The outline of the computational procedure indicating the software used during each step of the optimisation (oval = start/end, parallelogram = input/output, rectangle = process, diamond = decision).

2.4 Honeycomb fabrication

Additive manufacturing was employed to fabricate the honeycombs identified through the optimisation. Figure 6 illustrates the computer aided design files, generated using a python script, were converted to .stl file format for interpretation by the laser sintering machine. Fabrication was sub-contracted to a specialist third party, building parts from Luvosint X92A-1 (Lehmann & Voss & Co; Hamburg, Germany) a thermoplastic polyurethane powder described in section 2.2. A contouring scan mode was leveraged with a minimum layer thickness in the z direction was set to 0.1mm. Post processing was performed using compressed air to remove excess unsintered powder. Build accuracy was assessed by measuring finished parts using a Vernier Calliper (Absolute AOS Digimatic, Mitutoyo, Japan), for comparison to the intended design values.

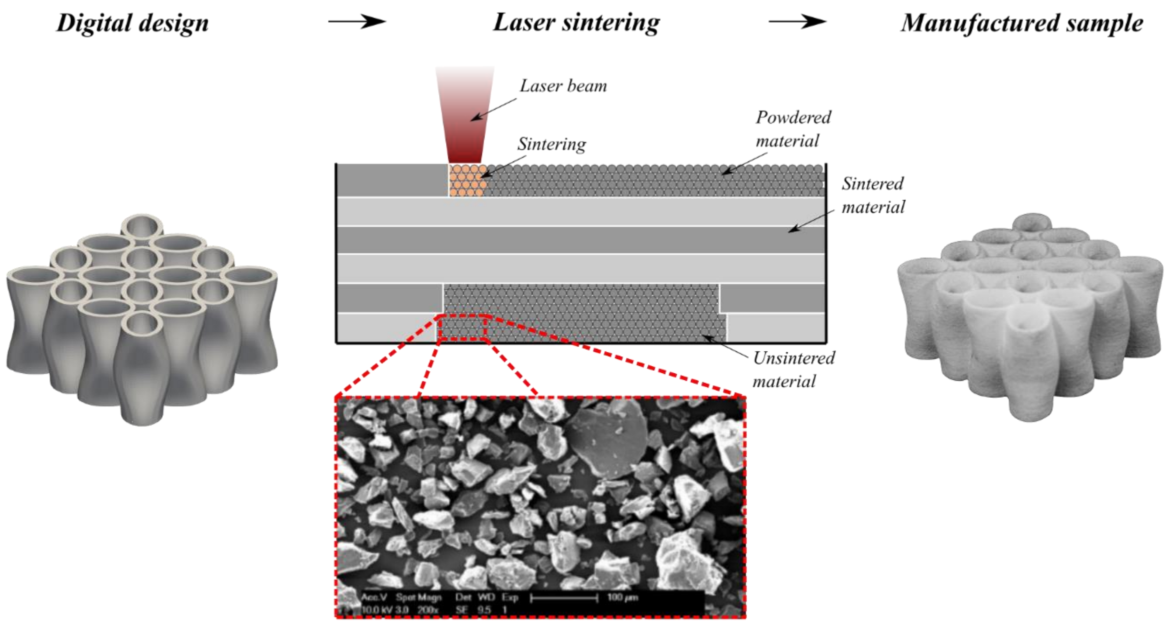

Figure 6: The fabrication method for the optimal honeycomb design including digital design, laser sintering overview and final part. Scanning electron imagery of Luvosint powder has been adopted from [43]

2.5 Experimental validation

Fabricated honeycombs were subjected to dynamic impact loading, to validate the results of the numerical optimisation procedure. This was performed using a monorail shock absorption testing facility (model: 1002 MAU 1006/CF/ALU; AD Engineering, Italy) (figure 7). Each honeycomb was taped to the upper platen of the drop carriage, which was designed specifically to have an equivalent mass to a size J headform (4.7kg). The carriage was then wire-guided, under free-fall, onto a steel anvil that had a 50kN load cell positioned within it. Each sample was subjected to an initial impact velocity of 5.42m/s validated through use of a light gate. Data was recorded at 50,000Hz and treated with a low pass Butterworth filter that had a 1000Hz cut-off frequency. The line of impact was out-of-plane to the build orientation. All testing was performed in ambient conditions.

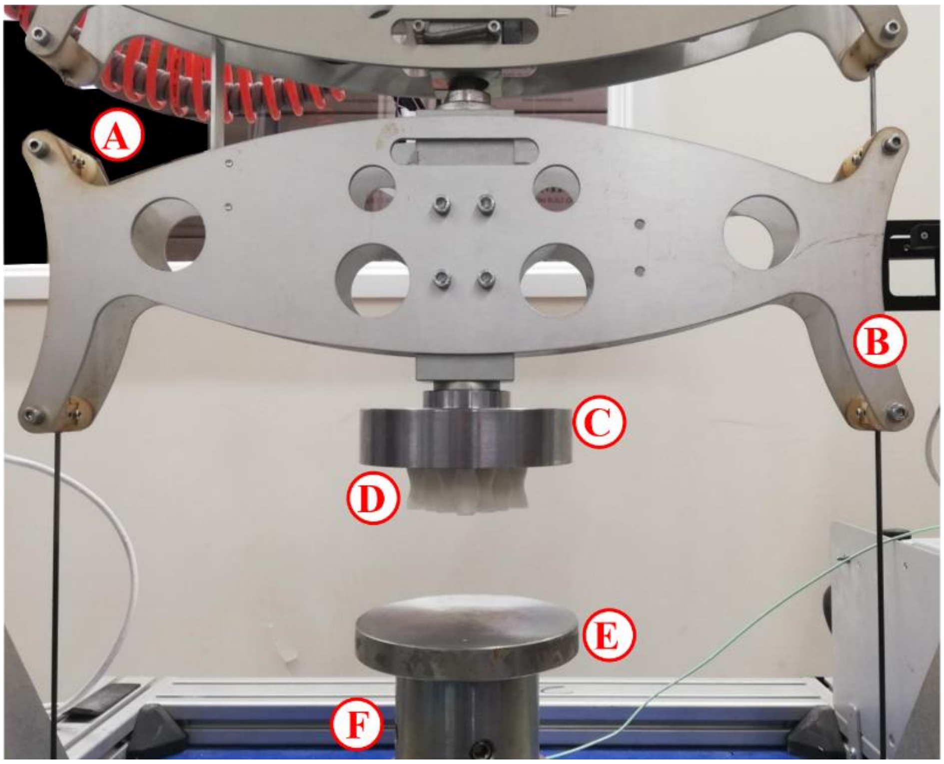

Figure 7: The experimental setup for impact testing of the optimised honeycomb samples including drop carriage (A), light gate (B), upper plate (C), honeycomb sample (D), lower plate (E), load cell (F).

3. Results

In this section, the results from the numerical optimisation are presented. The variation in honeycomb impact behaviour is reported relative to the number of function evaluations as well as changing the objective function. Variation in objective function relative to structural parameters is also discussed. Following, fabricated samples are subject to experimental testing to validate the outcome of the numerical optimisation. Lastly, testing is carried out over successive repeats to explore the multi-impact behaviour and performance degradation of the fabricated honeycombs.

3.1 Optimisation

Figure 8 reports the variation in the objective function, peak linear acceleration (PLA), for each evaluation relative to the acceptable 250g limit during the optimisation. The optimisation procedure successfully satisfied the objective function yielding a response less than 250g. The first 20 evaluations are randomly sampled yielding a variation in objective function between 419.7 and 158.0g. The minimum value reported in the random sample was at iteration 9. This represents a relative reduction in the objective function by 36.8%. The optimal solution was identified during the first surrogate, within the adaptive sampling phase between iterations 20 and 75. The minimum solution reported was 140g at the 56th evaluation representing a further reduction by 11.4% compared to the best point of the random sample. To ensure that the current best point was the global minimum, the surrogate model was reset after the 75th iteration and random sampling was undertaken to construct a new surrogate. The surrogate reset failed to achieve an improvement on the best point from the first surrogate. Similarly, a third and final reset (started at 125th iteration) also failed to achieve an improvement, although the procedure was terminated prior to reaching adaptive sampling as the maximum number of iterations had been exceeded (i_{max} = 150).

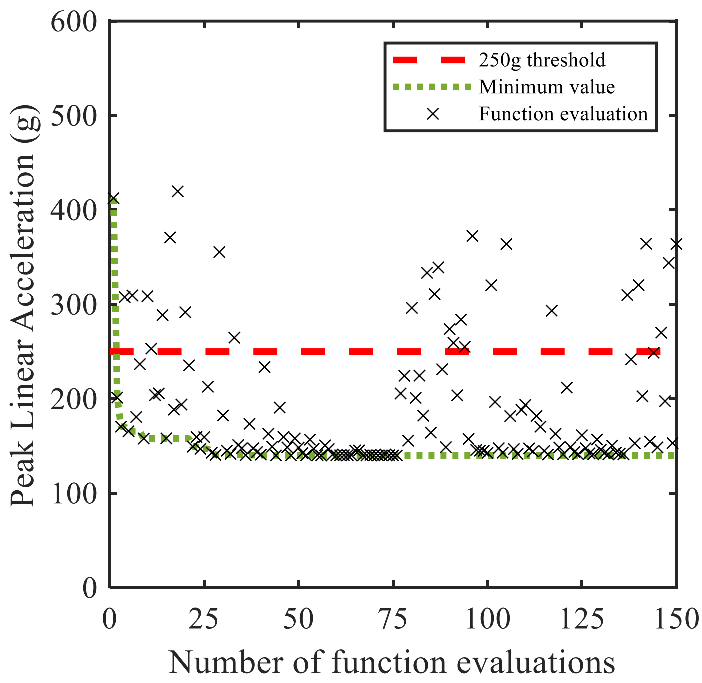

Figure 8: The variation in the objective function, peak linear acceleration, for each function evaluation relative to a threshold of 250g

Figure 9a – 9c illustrates the changing resultant acceleration and mechanical behaviour of the honeycomb during the optimisation procedure. Comparison is made to the acceptable shock absorption threshold of the design standard, as well as the failure criterion for skull fracture [44]. Iterations 1, 14 and 56, of the first surrogate model, are reported as they demonstrate two characteristic behaviours and the optimal result. Iteration 1 represents an overly compliant response. As the structure begins to deform, buckling occurs at a relatively low stress, initially resulting in a low acceleration. As the structure proceeds through the plateau region, the structure fails to sufficiently mitigate the kinetic energy of the impactor. Consequently, the structure begins to densify yielding a large and rapid increase in acceleration, exceeding the acceptable threshold, as the impact is mitigated through compression of the base material. The duration of the impact occurs over 9ms, reaching a PLA of 412g, and a peak stress of 7.6MPa. Conversely, iteration 14 represents an overly stiff response. The structure deforms at a high stress, yielding a high initial acceleration, which exceeds the permissible threshold. By the time the structure buckles, entering the non-linear region before the plateau phase, the kinetic energy of the impact has been mitigated leading towards a response which is over in less than 6ms reaching a PLA of 288g, and a peak stress of 5.3MPa. Iteration 56 represents the optimal solution. The response effectively mitigates the kinetic energy prior to reaching the onset of densification, without exceeding the 250g threshold. Buckling occurs at a stress that is below the acceptable threshold; whilst structural stress-softening is observed, acceleration remains nearly constant throughout.

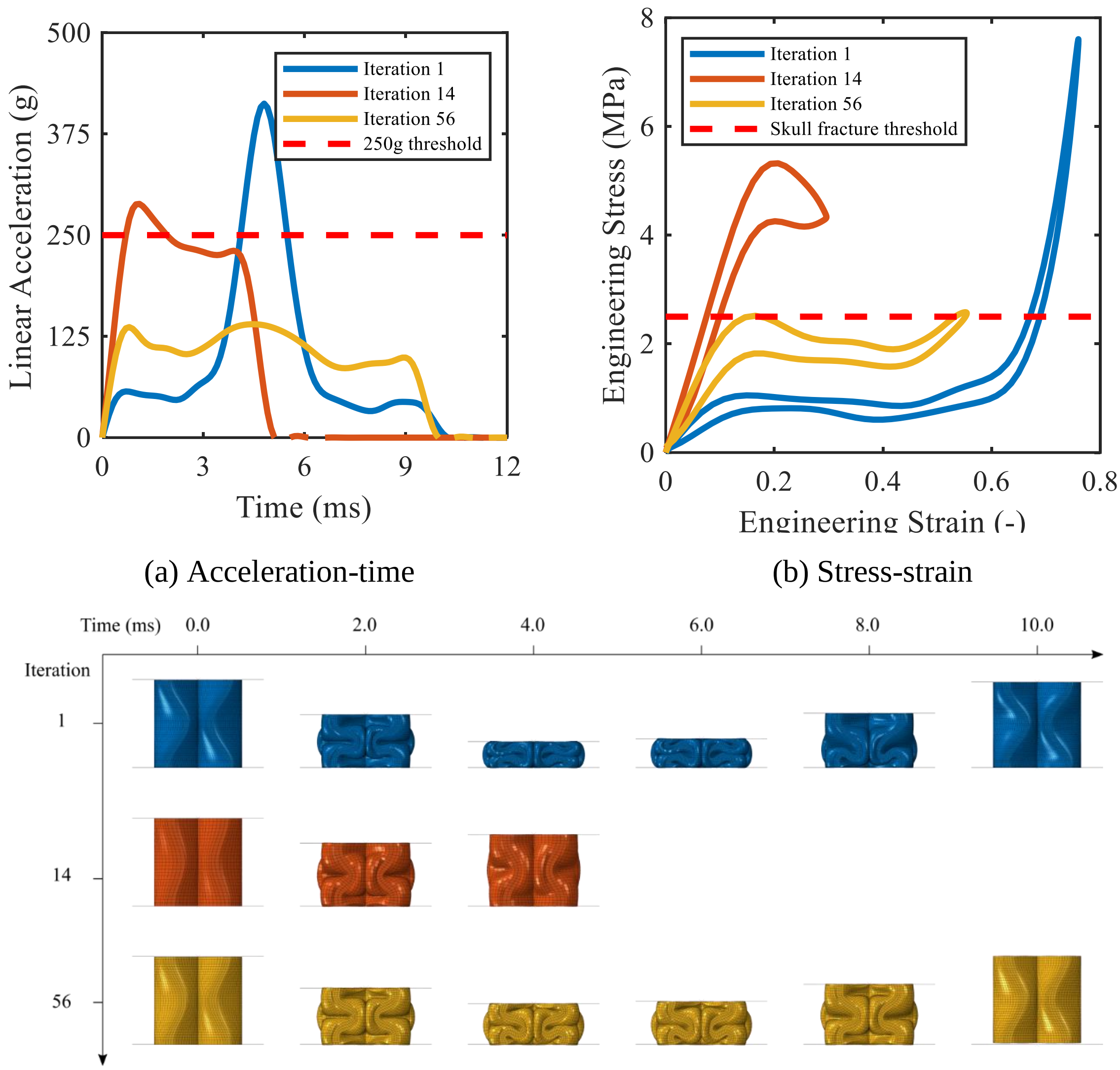

(a) Acceleration-time

(b) Stress-strain

(c) Visualised deformation with respect to time

Figure 9: The simulated response for iterations 1, 14 and 56 for the optimisation where PLA was the objective function

Figure 10 further examines the data recorded in the optimisation procedure. In addition to PLA, HIC was calculated at each function evaluation; the variation in PLA and HIC is reported at each function evaluation. The data features two trends constructed in a slanted 'V-shape'. Firstly, the left-hand side trend ranges between 140 to 412g, within which the value for HIC varies between 1129 to 3024. Conversely, for a similar PLA range, the associated right-hand HIC values range from 1129 to 5658. These two trends meet at a point of intersection located at the bottom left-hand corner. The density of function evaluations in this region, compared to the others, is indicative of the location of the identified minimum. The ‘V-shape’ formulation of data reports an interesting feature, where points of equivalent PLA have markedly different HIC. One such instance is reported in figure 11a and 11b, which compares the acceleration-time and mechanical behaviour of these two points. Similar behaviour to that observed in 9a and 9b is observed i.e., a stiff structure that mitigates the kinetic energy prior to reaching the plateau, versus a compliant structure that mitigates kinetic energy by deforming within the plateau and densification region. Interestingly the search algorithm qualifies both results equally based on the PLA reported, however, the calculated HIC values are markedly different. Notably, the HIC value for the stiff structure is 114.1% greater than the compliant structure. Since the search algorithm examines these two responses equally, a greater number of iterations is required to attain the optimum solution. In both cases the requirement of the design standard (PLA < 250g), and thus objective function have been satisfied; however, owing to the significance of HIC as an injury severity index, it is prudent for further optimisation to consider HIC as the objective function.

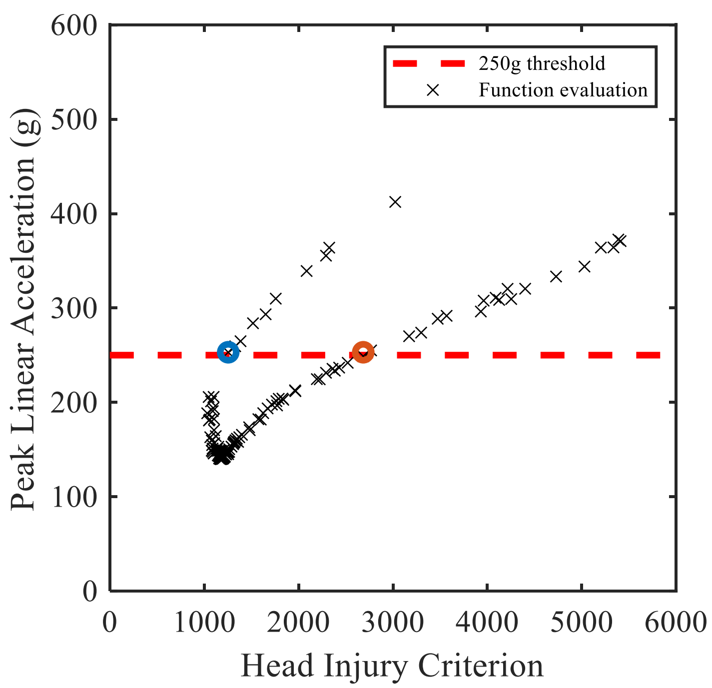

Figure 10: The variation in peak linear acceleration and head injury criterion at each function evaluation. Two points of equivalent PLA are indicated on the plot to be used in reference to figure 9.

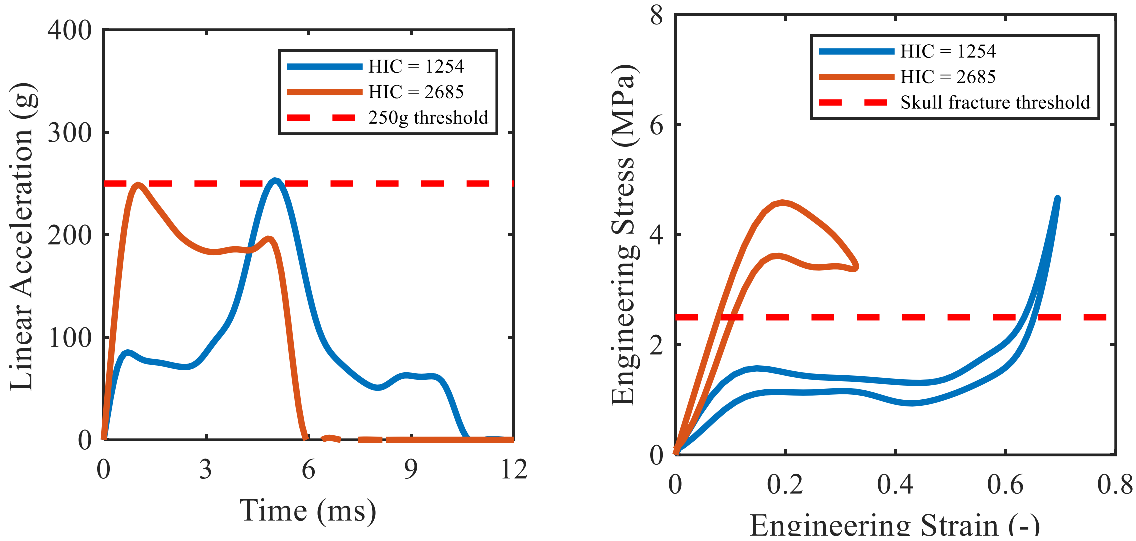

(a) Acceleration-time (b) Stress-strain

Figure 11: The comparison of impact response and mechanical behaviour of iteration 11 and 136, identified from figure 8, response when yielding the same peak linear acceleration

Figure 12 compares the objective function relative to the structural parameters, wall thickness and aspect ratio. The contour plot illustrates a band of minimum peak linear acceleration, neighboured equally either side by areas of increasing values indicating that the results are forming a valley shape where the minima is located within the gulley. The two localised clusters of function evaluations are representative of the completed adaptive sample phases. The optimal values found for each surrogate were within 1% of each other. This suggests that for the pre-buckled honeycomb structure there is a band of optimal values for various combinations of wall thickness and aspect ratio as indicated by the dashed lines. Within this band of near contact performance for decreasing aspect ratio an increase in wall thickness is required to mitigate the impact.

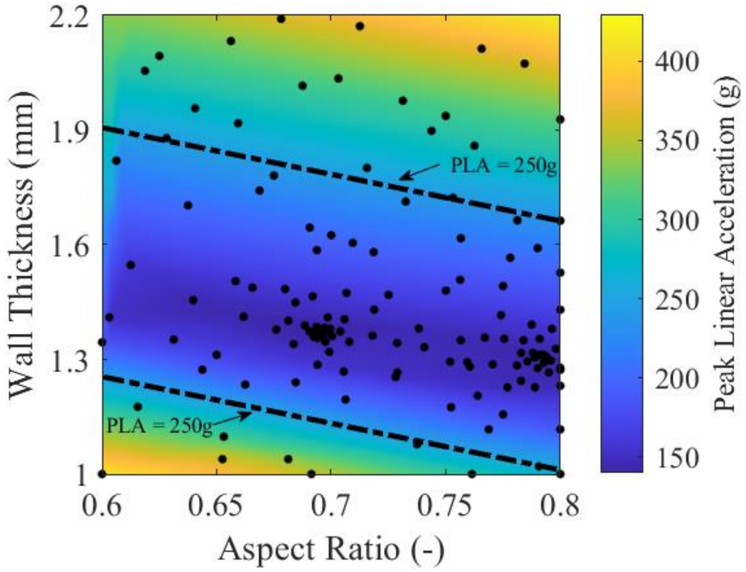

Figure 12: The variation in peak linear acceleration relative to wall thickness and aspect ratio when the objective function is set to PLA. Each function evaluation is indicated by a black point.

To examine the influence of objective function, HIC was used in a secondary optimisation. Considering equation (1), the objective was calculated and normalised by a value of HIC = 1574, equivalent to an abbreviated injury score (AIS) of 4, whilst all other optimisation and structural parameters remained the same. Figure 13 reports the variation in objective function, HIC, for each evaluation relative to the new acceptable threshold during the optimisation. The optimisation procedure successfully satisfied the objective function yielding a response with a HIC less than 1574. The first 20 evaluations are randomly sampled yielding a variation in HIC between 5412 and 1050. The minimum value reported in the random sample was at iteration 7. This represents a reduction in the objective function by 33.3%. The minimum solution was identified during the adaptive solution between iterations 20 to 85. The minimum solution reported was HIC = 1029 at the 48th evaluation representing a reduction of 2.0% compared to the best point of the random sample. Subsequent function evaluations do not yield an improved result. After the 90th function evaluation the surrogate model is reset and random sampling occurs again to construct the surrogate model, however, this search does not attain improvement.

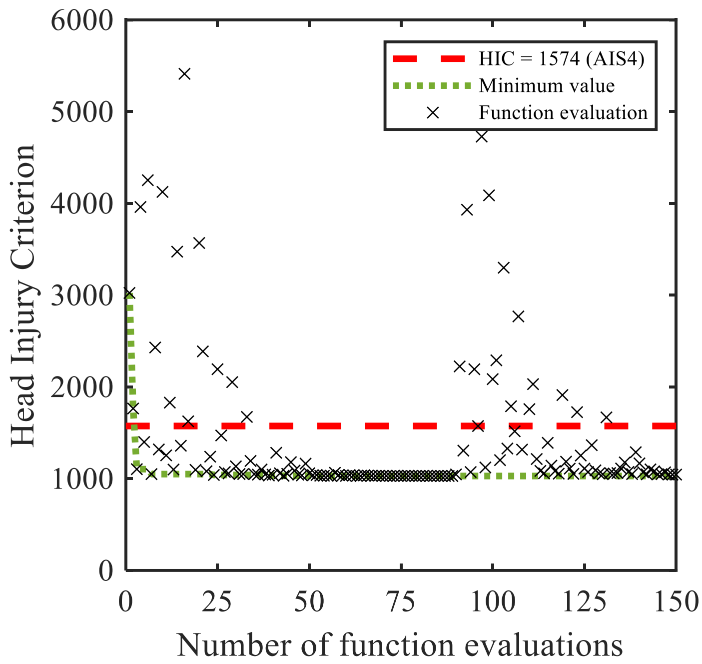

Figure 13: The variation in the objective function, head injury criterion, for each function evaluation relative to a threshold of 1574.

Figure 14 compares the objective function, HIC, relative to the structural parameters of wall thickness and aspect ratio. The contour plot illustrates a similar trend to figure 12. Figure 15 compares the optimal results from the PLA and HIC optimisation, hereafter referred to as PLA_{opt} and HIC_{opt} respectively. The objective function has a notable influence on the resultant mechanical response of the honeycomb. Specifically, the PLA_{opt} favours a higher yield and plateau stress than HIC_{opt}. Conversely HIC_{opt} favours a lower yield stress and takes advantage of densification. The reported PLA and HIC values for each optimal are reported in table 1.

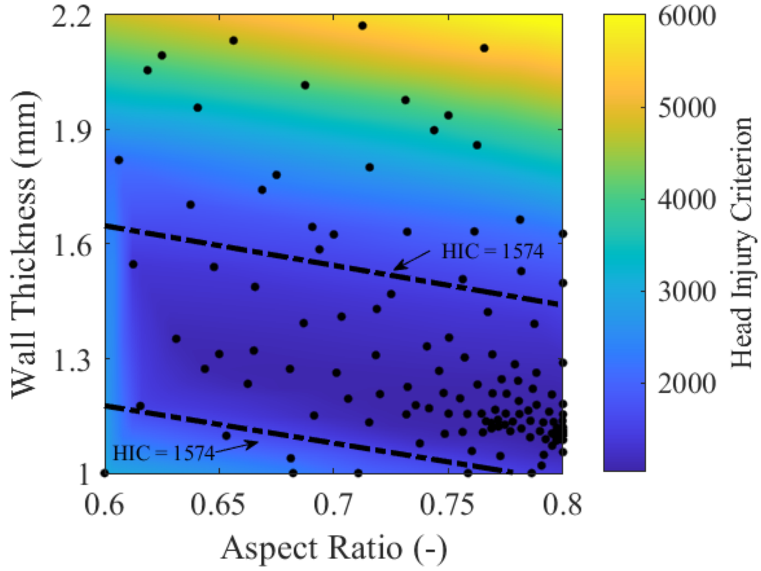

Figure 14: The variation in head injury criterion relative to wall thickness and aspect ratio when the objective function is set to PLA. Each function evaluation is indicated by a black point

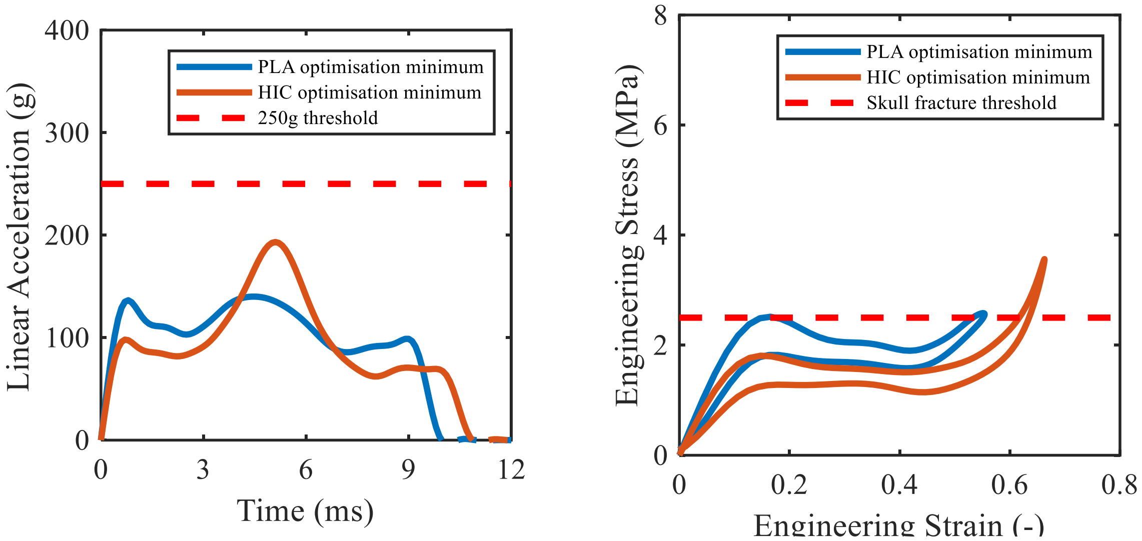

(a) Acceleration-time

(b) Stress-strain

Figure 15: Comparison of mechanical behaviour for optimal honeycombs based on an objective function of PLA and HIC.

Table 1: Structural and performance parameters for the optimal values for both objective functions.

Objective function	**Cell width (mm)**	**Wall thickness, t (mm)**	**Aspect ratio, e**	**Number of folds, f**	**PLA (g)**	**HIC**
PLA	12.5	1.37	0.70	1.0	140.0	1174
HIC	12.5	1.11	0.80	1.0	193.2	1029

3.2 Experimental validation

Sample inspection

As previously discussed, the optimised honeycomb structures were fabricated using laser sintering. The wall thickness was measured across 16 positions as well as overall length, width and height for each specimen. The values were then averaged and compared to the CAD models as reported by table 2. Visual inspection of the samples did not identify any defects due to residual stresses from the sintering process, such as warping or curling [45].

Table 2: Recorded dimensions of the fabricated honeycomb samples, difference from design values provided in brackets.

Label	**Average wall thickness (mm)**	**Sample length (mm)**	**Sample width (mm)**	**Sample height (mm)**
PLA_{opt}	1.42 (0.05)	50.05 (0.05)	50.02 (0.02)	25.04 (0.04)
HIC_{opt}	1.06 (-0.05)	49.62 (-0.38)	49.32 (0.68)	26.08 (1.08)

Single impact

Impact loading was performed on the fabricated honeycombs to demonstrate that the optimisation process yields structures which satisfy their objective functions. Figure 17a and 17b reports the acceleration-time data for the PLA_{opt} and HIC_{opt}. The PLA_{opt} solution satisfies its objective function, yielding a PLA value of 232.2g. This represents a relative decrease of 7.1% compared to the threshold value. The PLA_{opt} solution also satisfies the HIC objective function, yielding a value of 1274 and representing a relative decrease of 19.1%. The HIC_{opt} solution also satisfies its objective function, yielding a HIC value of 1085, which is a relative decrease of 31.1% compared to the threshold value. The HIC_{opt} solution, however, did not satisfy the PLA_{opt} threshold. The recorded PLA was 258.6g which exceeds the threshold value by 3.4%.

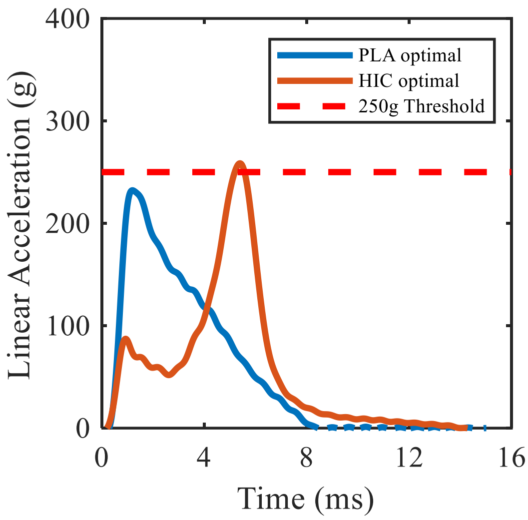

Figure 17: Experimental data of single impact loading for PLA and HIC optimised solutions

Repeat impact

Following the initial single impacts, each sample was subjected to 4 additional repeat impacts at 1-hour intervals to characterise the multiple loading behaviour of the optimal structures. Figure 18a and 18b reports the acceleration-time data for samples of PLA_{opt} and HIC_{opt} with respect to the first, third and firth repeat impact. Moreover, figure 18c and 18d reports the PLA and HIC values reported with respect to all repeat impacts.

The PLA_{opt} solution was optimised with respect to an objective function threshold of PLA < 250g. Following the second impact, the PLA recorded was 172.3g representing a relative reduction of 25.8%. For an increasing number of impacts an improvement in performance was observed. For impacts 3 – 5, a successive relative reduction of 8.5%, 1.8% and 2.5% is observed. Moreover, repeat impacts 4 and 5 represent a stabilised response when compared to impacts 1 – 3 which yields less variation and a more predictable response. Comparing the performance of the final impact (number 5), the reported value is 39.6% less than the objective function threshold (250g). The PLA_{opt} results also satisfies the HIC_{opt} objective function for repeat impacts. Similar to the PLA trends, the reported HIC values decreased for increasing number of impacts. For a single impact the reported HIC value was 1274. Following the second impact, the HIC value recorded was 945 representing a relative reduction of 25.8%. For impact 3 – 5, a successive reduction of 3.5%, 2.0% and 1.0% was observed. Comparing the performance of the final impact (number 5), the reported value was 29.9 % less than HIC_{opt} objective function threshold.

The HIC_{opt} solution was optimised with respect to an objective function of HIC < 1574. Following the second impact, the HIC recorded was 2723 representing a relative increase of 150.1%. For an increasing number of impacts a common trend of deteriorating performance is observed. For impacts 3-5, a successive increase of 32.6%, 12.1% and 8.9% is reported. Comparing the performance of the final impact (number 5), the reported value is 306.0% greater than the critical value. As previously discussed in the analysis of single impact behaviour, the HIC_{opt} solution does not satisfy the PLA_{opt} objective function. For the first repeat impact, the PLA recorded was 446.2g representing an increase of 72.5%. For an increasing number of impacts a common trend of deteriorating performance is observed. For impacts 3 – 5, a successive increase of 19.8%, 7.3% and 5.2% of PLA is reported. Comparing the performance of final impact (number 5), the reported value is 141.3% greater than the critical value (250g).

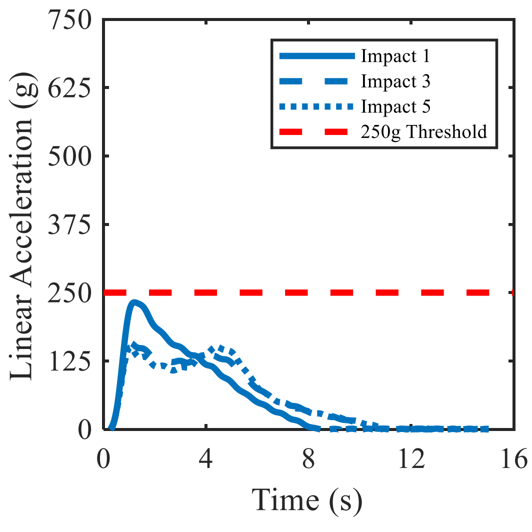

(a) PLA_{opt} acceleration-time

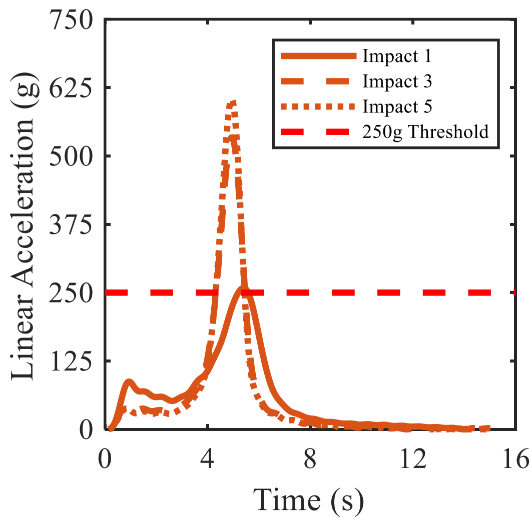

(b) HIC_{opt} acceleration-time

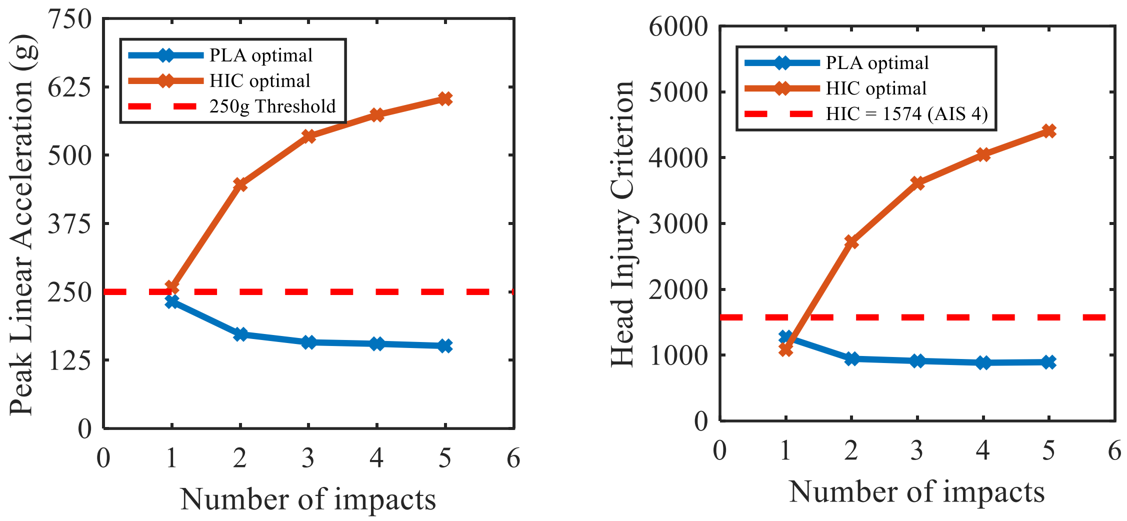

(c) Comparison of PLA (d) Comparison of HIC

Figure 18: Experimental comparison of repeat impact loading for PLA and HIC optimised solutions

4. Discussion

In this section, the effect of changing objective function is qualitatively analysed relative to the mechanical behaviour of the honeycomb. Following, experimental phenomena observed are related to structural and material-based energy absorption mechanisms of the honeycomb. Next, limitations in performance are reported before expanding on future applications of the optimisation process.

Finite element simulations were employed to obtain the resultant acceleration of the parametrised pre-buckled honeycomb structure when subject to impact loading. The surrogate optimisation algorithm from the MATLAB toolbox was used to analyse the results of FE simulation response relative to the design space. It was shown that the novel circular pre-buckled honeycomb design can minimise PLA and therefore satisfy the requirements of the design standard, but this was achieved at the expense of the HIC index. Varying the objective function from PLA to HIC resulted in notable differences in honeycomb response. The PLA optimal favoured a high yield and plateau stress, ensuring that the impact energy had been mitigated prior to entering densification, avoiding the characteristic large and rapid increase in acceleration. In contrast, the HIC optimal favoured a lower yield and plateau stress, resulting in densification of the structure. Since the structure yields at a lower comparative stress, the resultant acceleration is reduced in comparison to the PLA optimal. Once the structure densifies, however, the resultant acceleration exceeds that of the PLA optimal. This reduces the time of exposure to injurious levels of acceleration [46].

Experimental testing aimed to validate the numerically identified optimal configurations. Both structures, when tested experimentally, satisfied their respective objective function, however, the reported results did not match the numerical analysis. The HIC_{opt} configuration adopts a low yield stress which results in a reduced linear acceleration for a large proportion of the impact. It, however, takes advantage of the densification region to mitigate residual impact force for short periods at high acceleration. Consequently, there is a small operational window with which this structure works optimally. Variance in performance is therefore anticipated subject to variation in structural parameters. In this case variation in wall thickness, as reported by table 2, led to an overly compliant structure, meaning the structure was unable to sufficiently mitigate the impact. The negative performance was compounded over successive impacts, yielding a larger spike in acceleration as an increasing proportion of kinetic energy was mitigated within the densification region. Conversely, the wall thickness for the PLA_{opt} configuration exceeded the design value. Over successive impacts, the performance, however, improved. In both cases, repeat impact loading causes the base material to transition into its relaxed state due to cyclic stress softening [31] known as the Mullins effect . In the polymer's relaxed state, the resultant stress is lower for the same strain compared to the initial response. Considering the experimental PLA_{opt} results, the initial response was overly stiff, deforming at high stress and did not densify. The consequence of this was a larger resultant acceleration than that anticipated in the computational result. During the subsequent impacts, the structure deformed at lower stress due to the relaxation of the base material. The structure then proceeded to deform at a lower stress, yielding a reduced resultant acceleration whilst deforming further as characterised by nearly reaching densification. These results align with previous studies and indicates that there is opportunity for helmets to be pre-stressed (cycled / conditioned) to achieve repeatable, consistent behaviour [38]. This structure would be more long living than polymeric foams such as EPS, which tend to either plastically deform or demonstrate permanent set [25]. Consequently, this could benefit the user by reducing the risk of unknowingly wearing a helmet that is already damaged, from an innocuous drop or following an impact.

The finite element model used in this study consisted of a 2 x 2 array with a cell width of 12.5mm, representing a 4 x 4 array with a total contact area of 50 x 50mm equivalent to

$2500mm^2$. Contact area, however, is likely to change on a user-by-user basis as a function of head and helmet radii [47]. Previous investigations adopted a similar contact area values when investigating impact mitigation materials for helmet applications [32] although there seems to be little justification for this design choice. Moreover, other examples exist where a value as high as 6400 mm^2 has been used for similar impact conditions [48]. Increasing contact area for the same resistive force will yield a reduction in local stress exposed to the user. Therefore, selecting an appropriate contact area is paramount for future investigations. Analytical expression exists for the anticipated contact area based on helmet and head radius, and liner crush [49]. Considering general values for a size J headform, and a nominal liner crush of 0.5mm/mm for a 25mm liner, the contact area is in fact 10,000 mm^2. This exceeds the value used in this study, as well as previous studies, suggesting that an additional performance gain can be achieved through greater consideration of the anticipated contact area.

Whilst the optimised configurations satisfied the design standard performance threshold, the samples exceeded the typical mass of polymeric foam commonly used in helmet liners, 5g (80g/L [50]), by 10 - 20g. Adopting a stiffer base material with similar elasticity would allow use of thinner walls whilst enabling weight reduction and retaining performance. This could be achieved through different grades of powder [51], or inclusion of additives, such as functional reinforcement [52] and infiltration of resin [53] to improve the base material mechanical properties. Consequently, there is potential for further improvements in performance through adoption of additives within laser sintering to fabricate the pre-buckled honeycomb structure for multi-use helmet liner development.

The current optimisation process is guided by the design standards that prescribe a vertical impact and a minimum acceptable level of protection.-This, however, is contrary to the fact that the most commonly occurring helmet impact occur at an angle [54]. The forces that arise, therefore, have components of compression and shear [55], [56], [57] which ultimately leads to a rotational velocity and acceleration. It is widely accepted that the human head is susceptible to rotational kinematics [58] and that these loading regimes are more closely linked to traumatic brain injury [59], [60]. Consequently, future optimisation should include angled impact conditions as well as consider other head impact variables such as velocity, location, and curvature of the head.

5. Conclusion

In this study, an effective combined numerical framework was reported for optimisation of a parametrically defined honeycomb-type structure, subject to the boundary conditions of a common helmet design standard. Numerical optimisation was realised through use of an algorithm derived from a radial basis function based on finite element analysis, to form a surrogate model of the impact performance relative to the honeycomb's structural parameters. Samples were fabricated using laser sintering of a thermoplastic polyurethane powder , subjected to experimental impact conditions to validate the outcome of the numerical analysis, then to successive impacts to explore multi-impact behaviour and performance degradation.

Numerical optimisation revealed the influence of objective function on the impact behaviour for this class of additively manufactured elastomeric honeycomb. For the limits prescribed in the analysis, optimising for peak linear acceleration resulted in a structure that mitigates the kinetic energy of the impact at a stress which facilitates avoidance of the densification region. In contrast, optimising for head injury criterion results in a structure which yields at a relatively lower yield stress and resultant acceleration, however, densifies thus resulting in a higher peak linear acceleration but for a small duration. Fabrication and experimental testing of the samples provided further insights regarding the impact performance. Both structures satisfied their respective objective function when subjected to experimental testing, therefore providing validity for the numerical procedure and its adoption in future studies. Over repeat impacts, PLA optimised structures reported improved performance and stabilised after the third impact. performance was observed over multiple impacts, stabilizing after the third impact. In contrast, HIC optimised structures reported degrading performance over successive impacts. The culmination of this study is a numerical design pathway for exploring new materials and structures for head impact protection.

6. Acknowledgements

R. Adams' PhD is part-sponsored by COMFG Ltd. (Charles Owen, Royal Works, Croesfoel Ind. Park, Wrexham, LL14 4BJ, UK). S. Townsend was supported by a grant from the Head Health Tech V competition.

7. Appendix

Table A1: Hyperelastic material model coefficients (Ogden N5). Adopted from [37].

N	μ	α	D
1	903.01	3.72	0
2	-723.56	5.24	0
3	264.03	6.19	0
4	-669.43	2.26	0
5	236.66	1.42	0

Table A2: Linear viscoelastic material model coefficients (Prony series). Adopted from [37].

N	G	K	τ
1	0.16	0	1.35E-03
2	0.13	0	7.13E-02
3	8.98E-02	0	0.92
4	7.29E-02	0	6.27
5	8.04E-02	0	49.41

8. References

[1] D. S. McNally and S. Whitehead, “A computational simulation study of the influence of helmet wearing on head injury risk in adult cyclists,” *Accid. Anal. Prev.*, vol. 60, pp. 15–23, Nov. 2013.

[2] N. Dodds *et al.*, “Evaluating the impact of cycle helmet use on severe traumatic brain injury and death in a national cohort of over 11000 pedal cyclists: A retrospective study from the NHS England Trauma Audit and Research Network dataset,” *BMJ Open*, vol. 9, no. 9, p. e027845, Sep. 2019.

[3] A. E. Forbes, J. Schutzer-Weissmann, D. A. Menassa, and M. H. Wilson, “Head injury patterns in helmeted and non-helmeted cyclists admitted to a London Major Trauma Centre with serious head injury,” *PLoS One*, vol. 12, no. 9, p. e0185367, Sep. 2017.

[4] M. Bottlang, A. Rouhier, S. Tsai, J. Gregoire, and S. M. Madey, “Impact Performance Comparison of Advanced Bicycle Helmets with Dedicated Rotation-Damping Systems,” *Ann. Biomed. Eng.*, vol. 48, no. 1, pp. 68–78, Jan. 2020.

[5] A. F, D. K, Z. K, S. H, and G. M, “A New Assessment of Bicycle Helmets: The Brain Injury Mitigation Effects of New Technologies in Oblique Impacts,” *Ann. Biomed.*

Eng., 2021.

[6] “Helmets: a road safety manual for decision-makers and practitioners,” Geneva, 2006.

[7] D. C. Thompson, F. P. Rivara, and R. Thompson, “Helmets for preventing head and facial injuries in bicyclists.,” *Nurs. Times*, vol. 97, no. 43, p. 41, 2001.

[8] N. Melo, R. J. Berg, and K. Inaba, “Injuries sustained by bicyclists,” *Trauma*, vol. 16, no. 3, pp. 183–188, May 2014.

[9] A. S. McIntosh *et al.*, “Sports helmets now and in the future,” *Br. J. Sports Med.*, vol. 45, no. 16, pp. 1258–1265, Dec. 2011.

[10] S. P. Soe, P. Martin, M. Jones, M. Robinson, and P. Theobald, “Feasibility of optimising bicycle helmet design safety through the use of additive manufactured TPE cellular structures,” *Int. J. Adv. Manuf. Technol.*, vol. 79, no. 9–12, pp. 1975–1982, Mar. 2015.

[11] S. F. Khosroshahi, S. A. Tsampas, and U. Galvanetto, “Feasibility study on the use of a hierarchical lattice architecture for helmet liners,” *Mater. Today Commun.*, vol. 14, pp. 312–323, Mar. 2018.

[12] S. F. Khosroshahi, H. Duckworth, U. Galvanetto, and M. Ghajari, “The effects of topology and relative density of lattice liners on traumatic brain injury mitigation,” *J. Biomech.*, vol. 97, p. 109376, Dec. 2019.

[13] E. C. Clough, T. A. Plaisted, Z. C. Eckel, K. Cante, J. M. Hundley, and T. A. Schaedler, “Elastomeric Microlattice Impact Attenuators,” *Matter*, vol. 1, no. 6, pp. 1519–1531, Dec. 2019.

[14] L. J. Gibson and M. F. Ashby, *Cellular solids: Structure and properties, second edition*. Cambridge University Press, 2014.

[15] T. Thomas and G. Tiwari, “Crushing behavior of honeycomb structure: a review,” *Int. J. Crashworthiness*, 2019.

[16] Z. Wang, “Recent advances in novel metallic honeycomb structure,” *Composites Part B: Engineering*, vol. 166. Elsevier Ltd, pp. 731–741, 01-Jun-2019.

[17] F. Kholoosi and S. A. Galehdari, “Design, optimisation and analysis of a helmet made with graded honeycomb structure under impact load,” *Int. J. Crashworthiness*, vol. 24, no. 6, pp. 645–655, Nov. 2019.

[18] N. S. Ha and G. Lu, “Thin-walled corrugated structures: A review of crashworthiness designs and energy absorption characteristics,” *Thin-Walled Struct.*, vol. 157, p. 106995, Dec. 2020.

[19] S. Li, Z. Xiao, Y. Zhang, and Q. M. Li, “Impact analysis of a honeycomb-filled

motorcycle helmet based on coupled head-helmet modelling," *Int. J. Mech. Sci.*, vol. 199, p. 106406, Jun. 2021.

[20] G. D. Caserta, L. Iannucci, and U. Galvanetto, "Shock absorption performance of a motorbike helmet with honeycomb reinforced liner," *Compos. Struct.*, vol. 93, no. 11, pp. 2748–2759, 2011.

[21] E. Bliven *et al.*, "Evaluation of a novel bicycle helmet concept in oblique impact testing," *Accid. Anal. Prev.*, vol. 124, pp. 58–65, Mar. 2019.

[22] M. L. Bland, D. S. Zuby, B. C. Mueller, and S. Rowson, "Differences in the protective capabilities of bicycle helmets in real-world and standard-specified impact scenarios," *Traffic Inj. Prev.*, 2018.

[23] K. Hansen *et al.*, "Angular Impact Mitigation system for bicycle helmets to reduce head acceleration and risk of traumatic brain injury," *Accid. Anal. Prev.*, vol. 59, pp. 109–117, Oct. 2013.

[24] S. K. Bhudolia, G. Gohel, and K. F. Leong, "Enhanced energy absorption characteristics of novel integrated hybrid honeycomb/polystyrene foam," *J. Cell. Plast.*, Oct. 2020.

[25] C. G. Mattacola, C. Quintana, J. Crots, K. I. Tumlin, and S. Bonin, "Repeated impacts diminish the impact performance of equestrian helmets," *J. Sport Rehabil.*, vol. 28, no. 4, pp. 368–372, May 2019.

[26] R. J. Bromell and D. C. Geddis, "Child cyclists: A study of factors affecting their safety," *J. Paediatr. Child Health*, vol. 53, no. 2, pp. 145–148, Feb. 2017.

[27] B. Hanna *et al.*, "Auxetic Metamaterial Optimisation for Head Impact Mitigation in American Football," *Int. J. Impact Eng.*, p. 103991, Jul. 2021.

[28] C. Yang, H. D. Vora, and Y. Chang, "Behavior of auxetic structures under compression and impact forces," 2018.

[29] S. R. G. Bates, I. R. Farrow, and R. S. Trask, "3D printed polyurethane honeycombs for repeated tailored energy absorption," *Mater. Des.*, vol. 112, pp. 172–183, Dec. 2016.

[30] S. R. G. Bates, I. R. Farrow, and R. S. Trask, "Compressive behaviour of 3D printed thermoplastic polyurethane honeycombs with graded densities," *Mater. Des.*, vol. 162, pp. 130–142, 2019.

[31] R. Adams, S. Townsend, S. Soe, and P. Theobald, "Mechanical behaviour of additively manufactured elastomeric pre-buckled honeycombs under out-of-plane quasi-static and impact loading (Under Review By Journal)," *Mater. Des.*, vol. TBC.

[32] S. Townsend, R. Adams, M. Robinson, B. Hanna, and P. Theobald, "3D printed origami honeycombs with tailored out-of-plane energy absorption behavior," *Mater. Des.*, vol. 195, p. 108930, 2020.

[33] V. Caccese, J. R. Ferguson, and M. A. Edgecomb, "Optimal design of honeycomb material used to mitigate head impact," *Compos. Struct.*, vol. 100, pp. 404–412, Jun. 2013.

[34] T. Whyte *et al.*, "A Review of Impact Testing Methods for Headgear in Sports: Considerations for Improved Prevention of Head Injury Through Research and Standards," *J. Biomech. Eng.*, vol. 141, pp. 70803–70804, 2019.

[35] "BS EN 1078: Helmets for pedal cyclists and for users of skateboards and roller skates," London, 2012.

[36] "EN 960: Headforms for use in the testing of protective helmets," 2006.

[37] R. Adams *et al.*, "A novel pathway for efficient characterisation of additively manufactured thermoplastic elastomers," *Mater. Des.*, vol. 180, p. 107917, 2019.

[38] M. Robinson *et al.*, "Mechanical characterisation of additively manufactured elastomeric structures for variable strain rate applications," *Addit. Manuf.*, vol. 27, pp. 398–407, May 2019.

[39] F. F. Abayazid and M. Ghajari, "Material characterisation of additively manufactured elastomers at different strain rates and build orientations," *Addit. Manuf.*, vol. 33, p. 101160, May 2020.

[40] J. Hutchinson, M. J. Kaiser, and H. M. Lankarani, "The Head Injury Criterion (HIC) functional," *Appl. Math. Comput.*, vol. 96, no. 1, pp. 1–16, Oct. 1998.

[41] H.-M. Gutmann, "A Radial Basis Function Method for Global Optimization," *J. Glob. Optim. 2001 193*, vol. 19, no. 3, pp. 201–227, Mar. 2001.

[42] E. Acar, "Simultaneous optimization of shape parameters and weight factors in ensemble of radial basis functions," *Struct. Multidiscip. Optim.*, vol. 49, no. 6, pp. 969–978, Dec. 2014.

[43] L. Verbelen *et al.*, "Analysis of the material properties involved in laser sintering of thermoplastic polyurethane," *Addit. Manuf.*, vol. 15, pp. 12–19, May 2017.

[44] N. J. Mills, *Polymer Foams Handbook: Engineering and Biomechanics Applications and Design Guide*. 2007.

[45] F. Shen, W. Zhu, K. Zhou, and L. L. Ke, "Modeling the temperature, crystallization, and residual stress for selective laser sintering of polymeric powder," *Acta Mech.*, vol. 232, no. 9, pp. 3635–3653, 2021.

[46] J. Versace, “A review of the Severity Index,” in *SAE Technical Papers*, 1971.

[47] H. Mustafa, T. Y. Pang, T. Ellena, and S. H. Nasir, “Impact attenuation of user-centred bicycle helmet design with different foam densities,” in *Journal of Physics: Conference Series*, 2019, vol. 1150, no. 1.

[48] Y. Mosleh, J. Vander Sloten, B. Depreitere, and J. Ivens, “Novel Composite Foam Concept for Head Protection in Oblique Impacts,” *Adv. Eng. Mater.*, vol. 19, no. 10, p. 1700059, Oct. 2017.

[49] F. M. Shuaeib, A. M. S. Hamouda, M. M. Hamdan, R. S. Radin Umar, and M. S. J. Hashmi, “Motorcycle helmet: Part II. Materials and design issues,” *J. Mater. Process. Technol.*, vol. 123, no. 3, pp. 422–431, May 2002.

[50] N. J. Mills and A. Gilchrist, “Bicycle helmet design,” *Proc. Inst. Mech. Eng. Part L J. Mater. Des. Appl.*, vol. 220, no. 4, pp. 167–180, 2006.

[51] L. Verbelen *et al.*, “Analysis of the material properties involved in laser sintering of thermoplastic polyurethane,” *Addit. Manuf.*, vol. 15, pp. 12–19, May 2017.

[52] R. D. Goodridge, C. J. Tuck, and R. J. M. Hague, “Laser sintering of polyamides and other polymers,” *Prog. Mater. Sci.*, vol. 57, no. 2, pp. 229–267, Feb. 2012.

[53] Y. Wen *et al.*, “Enhancement of mechanical properties of metamaterial absorber based on selective laser sintering and infiltration techniques,” *Compos. Commun.*, vol. 21, p. 100373, Oct. 2020.

[54] N. Bourdet, C. Deck, R. P. Carreira, and R. Willinger, “Head impact conditions in the case of cyclist falls:,” *http://dx.doi.org/10.1177/1754337112442326*, vol. 226, no. 3–4, pp. 282–289, Apr. 2012.

[55] C. Ling, J. Ivens, P. Cardiff, and M. D. Gilchrist, “Deformation response of EPS foam under combined compression-shear loading. Part I: Experimental design and quasi-static tests,” *Int. J. Mech. Sci.*, vol. 144, pp. 480–489, Aug. 2018.

[56] N. Bailly, Y. Petit, J.-M. Desrosier, O. Laperriere, S. Langlois, and E. Wagnac, “Strain Rate Dependent Behavior of Vinyl Nitrile Helmet Foam in Compression and Combined Compression and Shear,” *Appl. Sci. 2020, Vol. 10, Page 8286*, vol. 10, no. 22, p. 8286, Nov. 2020.

[57] C. Ling, J. Ivens, P. Cardiff, and M. D. Gilchrist, “Deformation response of EPS foam under combined compression-shear loading. Part II: High strain rate dynamic tests,” *Int. J. Mech. Sci.*, vol. 145, pp. 9–23, Sep. 2018.

[58] A. H. S. Holbourn, “Mechanics of Head Injuries,” *Lancet*, vol. 242, no. 6267, pp. 438–441, Oct. 1943.

[59] G. TA, “Mechanisms of brain injury.,” *J. Emerg. Med.*, vol. 11 Suppl 1, no. SUPPL. 1, pp. 5–11, Jan. 1993.

[60] A. I. King, J. S. Ruan, C. Zhou, W. N. Hardy, and T. B. Khalil, “Recent Advances in Biomechanics of Brain Injury Research: A Review,” *https://home.liebertpub.com/neu*, vol. 12, no. 4, pp. 651–658, Jan. 2009.